AIMS Materials Science, 12(6): 1092–1106.
DOI: 10.3934/matersci.2025051
Received: 17 September 2025
Revised: 28 October 2025
Accepted: 12 November 2025
Published: 19 November 2025

https://www.aimspress.com/journal/Materials

Research article

Effect of post-weld heat treatment on microstructure and mechanical properties of alloy 52M cladding metal

Haiyang Zhu[1,2], Zuojin Qin[3], Changzheng Xu[4,*], Kun Liu[2,*] and Jiasheng Zou[2,*]

[1] School of Metallurgical Engineering, Suzhou Institute of Technology, Jiangsu University of Science and Technology, Suzhou 215600, China
[2] School of Materials Science and Engineering, Jiangsu University of Science and Technology, Zhenjiang 212000, China
[3] Guangxi Zhongyuan Machinery Co., Ltd., Liuzhou 545000, China
[4] Baowu Special Metallurgy Co., Ltd., Shanghai 200000, China

* **Correspondence:** Email: xuchangzheng@baosteel.com; liu_kun@163.com; zjzoujs@just.edu.cn.

Abstract: Alloy 52M cladding metals were fabricated on low-alloy steel plates using strip electrode submerged arc welding (SAW), followed by post-weld heat treatment (PWHT) at 610 °C for 24 h. The influence of PWHT on the microstructure, tensile properties, and impact toughness of the cladding metal was investigated. The results showed that cladding metals exhibited a cellular microstructure, with precipitated phases primarily composed of intragranular (Nb,Ti)C and intergranular $M_{23}C_6$. After PWHT, the $M_{23}C_6$ precipitates at grain boundaries coarsened from fine granules to a blocky morphology. This microstructural evolution led to a slight increase in tensile strength (from 578 to 589 MPa), accompanied by a minor reduction in plasticity and impact toughness; elongation decreased from 51% to 47%, and impact absorption energy dropped from 79 to 75 J. Additionally, the dimples on both the tensile and impact fracture surfaces of the PWHT cladding metal were smaller and shallower compared to those of the as-welded cladding metal.

Keywords: alloy 52M; cladding metal; PWHT; microstructure; mechanical properties

1. Introduction

In pressurized water reactor (PWR) nuclear power plants, steam generators serve as critical boundaries separating the reactor coolant system (primary loop) from the power conversion system (secondary loop) [1–3]. On one side, water in the secondary loop undergoes heat exchange and a separation process inside the steam generator to produce dry steam; this steam then drives the turbine to generate electricity. On the other side, the steam generator acts as a crucial barrier, effectively preventing the leakage of radioactive heat transfer media from the primary loop. Notably, the tubesheet of the steam generator constitutes the pressure-retaining boundary between the primary and secondary loops. It operates in a harsh environment characterized by high temperature and pressure, while remaining in long-term contact with the radioactive and corrosive media present in the primary loop [4]. Tubesheets are commonly made from low-alloy steels, such as 18MND5 (RCC-M specification) or SA508 Gr.3 Cl.2 (ASME specification), due to their favorable mechanical properties and cost-effectiveness [5]. However, low-alloy steels exhibit poor corrosion resistance. To enhance corrosion protection, corrosion-resistant nickel-based overlays with a specified thickness are deposited on the primary-side surface of tubesheets [6]. In the early stages, nickel-based alloy 182/82 was used as the cladding material for the protective overlay on tubesheet surfaces. Nevertheless, the low-chromium (Cr) content nickel-based alloy 600 series was prone to stress corrosion cracking (SCC). It was therefore replaced by alloy 152/52, which is characterized by a higher Cr content (30 wt.%) and superior weldability. The composition of alloy 152/52 has been further optimized to improve its resistance to ductility-dip cracking (DCC), leading to the development of a new alloy, alloy 52M (known as NiCrFe-7A), which has now been widely adopted [7–9].

Common overlay welding technologies for nickel-based alloy materials include wire arc cladding [10], strip submerged arc cladding [11], and strip electroslag cladding [12]. Compared to wire cladding, strip cladding offers distinct advantages. These include uniform weld penetration, low base metal dilution, and high production efficiency [13]. As an efficient cladding method, strip cladding has been widely applied for manufacturing steam generators in recent years. For instance, Inconel weld strip 52M (EQNiCrFe-7A), paired with the submerged arc cladding flux Incoflux SAS2, has been widely used in tubesheet overlays [14].

Owing to the large cladding area, high heat input, and significant difference in thermal expansion coefficient between the nickel-based alloy cladding layer and the tubesheet base material, significant residual stress is likely to develop [15]. Consequently, post-weld heat treatment (PWHT) is necessary after cladding. Xu et al. [14] investigated the effect of PWHT on microstructural evolution and SCC resistance at the dissimilar metal interface of submerged-arc-welded alloy 52M overlay on low-alloy steel SA508 Gr.3 Cl.2. However, research focusing on the influence of PWHT on the microstructure and mechanical properties of cladding metal has been scarcely reported so far. In this study, Inconel 52M overlays were deposited on low-alloy steel using strip submerged arc cladding, followed by PWHT at 610 °C for 24 h. The variations in microstructure and mechanical properties of cladding metal after PWHT were characterized and analyzed.

2. Materials and methods

2.1. Sample preparation

The nickel-based cladding metals were fabricated on a low-alloy plate using a strip electrode submerged arc welding (SAW) process. The welding operation was conducted with a Lincoln DC1000/NA-5 power source, and the welding process is illustrated in Figure 1. A weld strip with rectangular cross-section serves as both the electrode and filler material. The arc burned beneath the flux cladding layer, and the molten flux formed slag and protective gas, which stabilized the arc and improved the formation quality of the cladding layer.

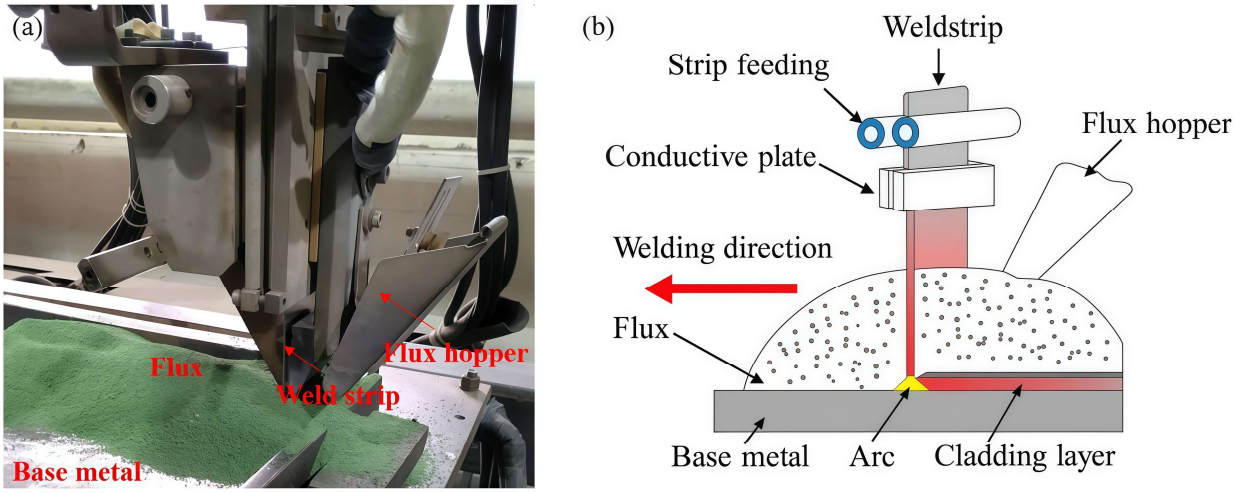

Figure 1. SAW process: (a) physical photograph, (b) schematic diagram.

The dimensions of the low-alloy base metal were 450 × 350 × 50 mm. The welding consumables included Inconel weld strip 52M (60 × 0.5 mm) paired with Incoflux SAS2. The composition of the weld strip 52M is presented in Table 1.

Table 1. Composition of weld strip 52M (wt.%).

Alloy	C	Si	Mn	Cr	Fe	Nb	Ti	Al	Ni
Weld strip 52M	0.03	0.12	0.78	30.24	8.70	0.79	0.20	0.14	Bal.

The cladding metal was applied in two passes per layer. Each layer had an interpass overlap of 15 mm. A total of 8 layers (16 passes) were deposited to achieve the final cladding dimension of 300 × 110 × 25 mm, as shown in Figure 2. The welding process parameters are presented in Table 2. Two cladding metals were welded using identical welding parameters. PWHT was then applied to one cladding metal to relieve internal stress. The PWHT parameters are shown in Figure 3. The test plate was loaded into the heat treatment furnace at 300 °C. The heating rate between 300 and 610 °C was 50 °C/h, followed by a 24 h holding time at 610 °C. Subsequently, the furnace was cooled at a rate of 50 °C/h.

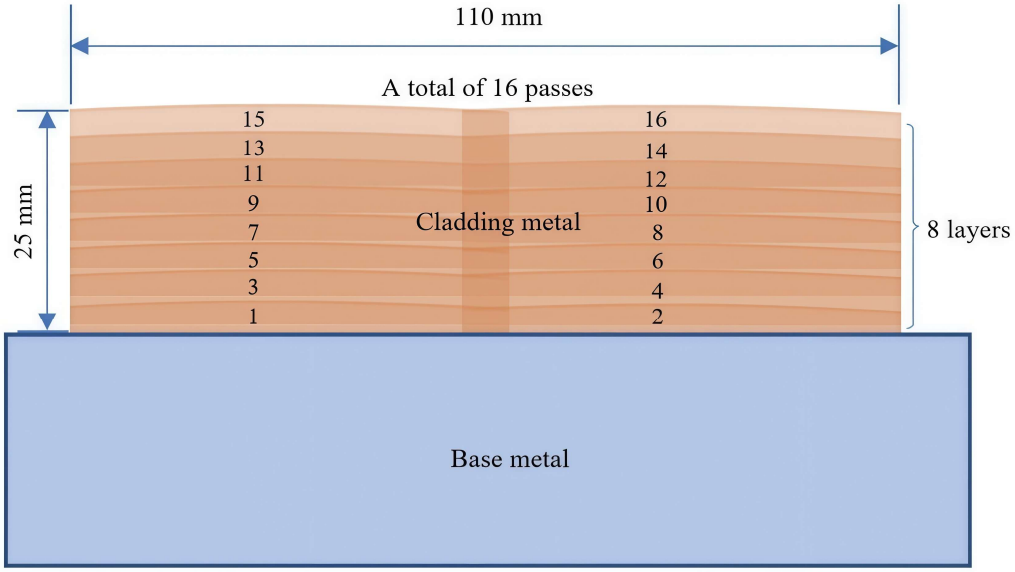

Figure 2. Schematic diagram of the welding procedure.

Table 2. Welding process parameters.

Current (A)	Voltage (V)	Speed (mm/min)	Interpass temperature (°C)
760	30	200	≤200

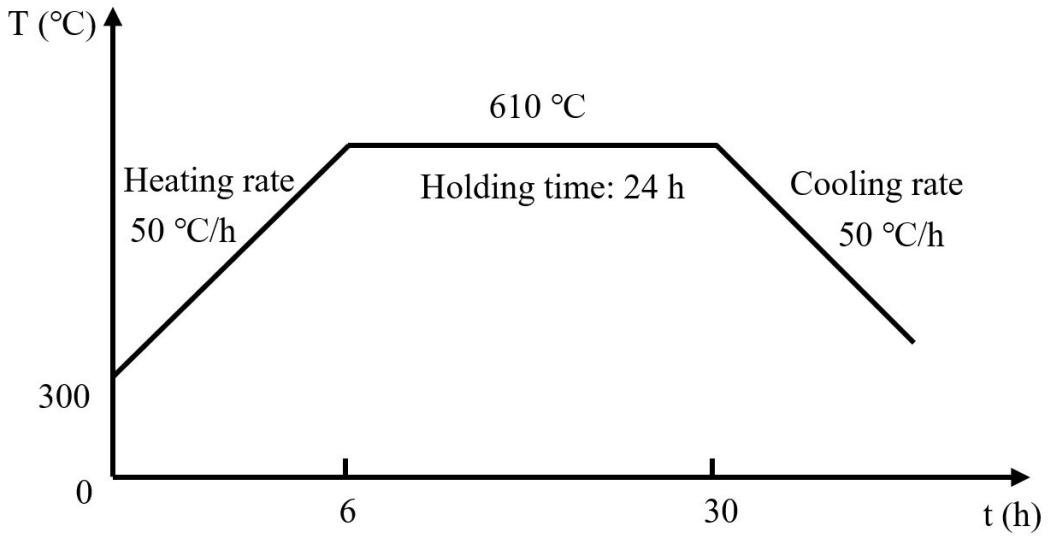

Figure 3. PWHT parameters.

2.2. Test method

The microstructure, tensile performance, and impact toughness of the cladding metals in as-welded and PWHT conditions were analyzed. The sampling location and specimen dimensions are shown in Figure 4. Two tensile specimens were prepared along the cladding metal's longitudinal direction, and three impact specimens were cut perpendicular to it for each metal. After mechanical grinding and

polishing, the metallographic specimens were etched for 10 s utilizing a solution prepared with 10 g of $CuSO_4$, 50 mL of HCl, and 50 mL of H_2O. Microstructure characterization was conducted using an optical microscope (OM) and a scanning electron microscope (SEM) equipped with an energy-dispersive spectrometer (EDS). A tensile test was performed at room temperature with a tensile rate of 1 mm/min. A Charpy V-notch impact test was carried out at room temperature using a pendulum impact testing machine. The fracture mechanisms of the tensile and impact fracture morphologies were analyzed by SEM.

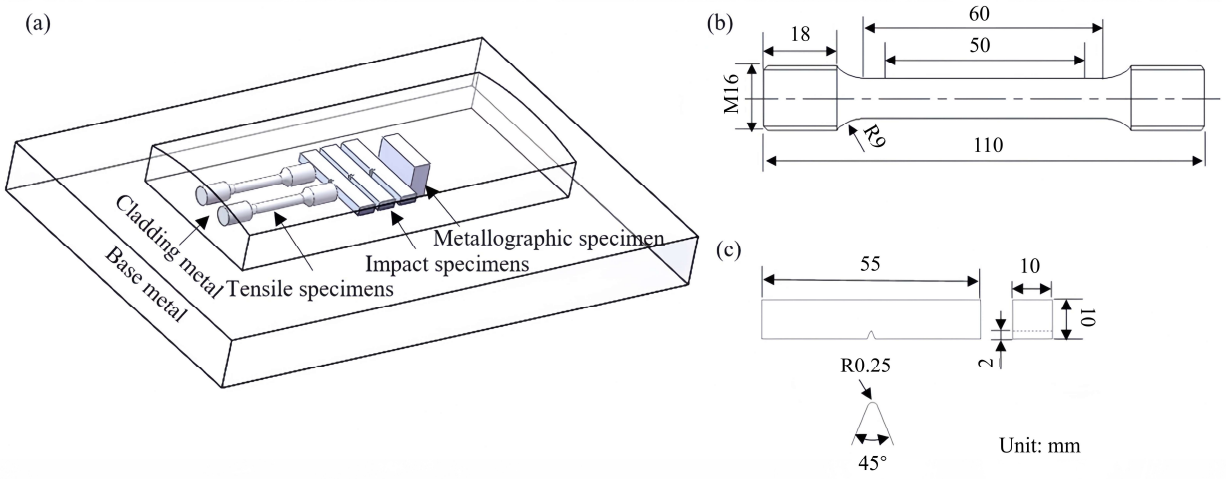

Figure 4. (a) Schematic of sampling position. (b) Tensile specimen dimensions. (c) Impact specimen dimensions.

3. Results and discussion

3.1. Microstructure

The microstructure at the middle region of cladding metals with as-welded and PWHT states is shown in Figure 5. Figure 5a shows that the microstructure of the as-welded cladding metal consists of a cellular crystal structure. As the metal solidifies, its solidification can proceed in a planar, cellular, or dendritic mode, and which of these modes occurs is determined by the solidification condition. The temperature gradient (G) and solidification rate (R) play a critical role in determining the solidification morphology. A low temperature gradient combined with a moderate solidification rate promotes the formation of cellular grains [16]. During the cladding process, the combination of high welding current and low cladding speed resulted in a reduced G and a moderate R, which promoted the formation of cellular grain structures rather than dendritic or planar growth morphologies. The cellular grains appeared equiaxed in the cross-section perpendicular to the heat flow direction but elongated in the parallel direction. Figure 5b shows a high-magnification microstructure image of the as-welded cladding metal. It can be seen that the grains are longer in one length direction and narrower in the other perpendicular direction, and there are a number of granular precipitates in the grains.

Figure 5c,d show the microstructure of the PWHT cladding metal. Compared with the as-welded state, the cellular crystal morphology remained unchanged, and the cellular crystal size also did not differ. Figure 6 presents the intragranular precipitate density, measured as the ratio of precipitate area to total area in Figure 5b,c using Image-Pro Plus software. The number of granular precipitates within

the grains changed only slightly. Experimental results showed that, using the same etching agent and duration, the grain boundaries of the PWHT cladding metal were more distinct than those of the as-welded cladding metal, which indicated that PWHT led to the coarsening of grain boundaries.

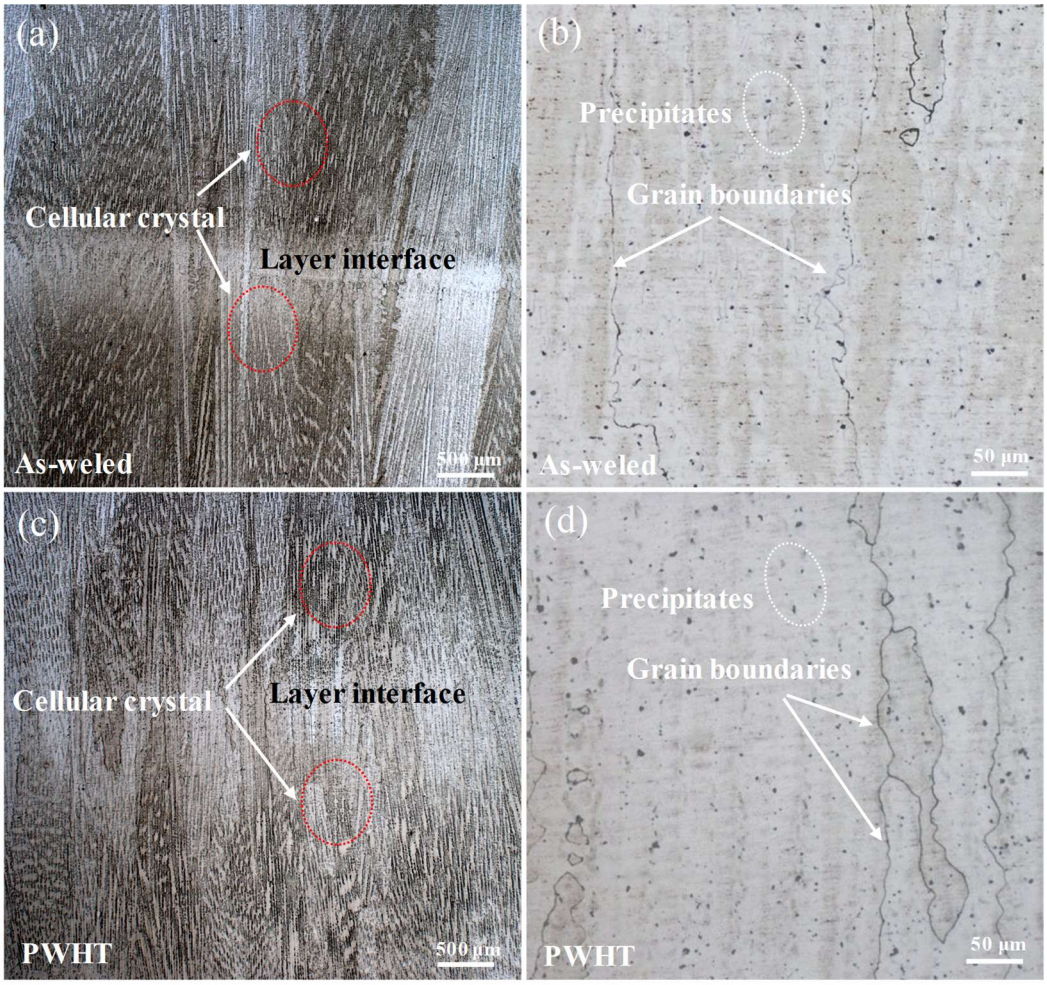

Figure 5. Microstructure of cladding metals: (a, b) as-welded condition; (c, d) PWHT condition.

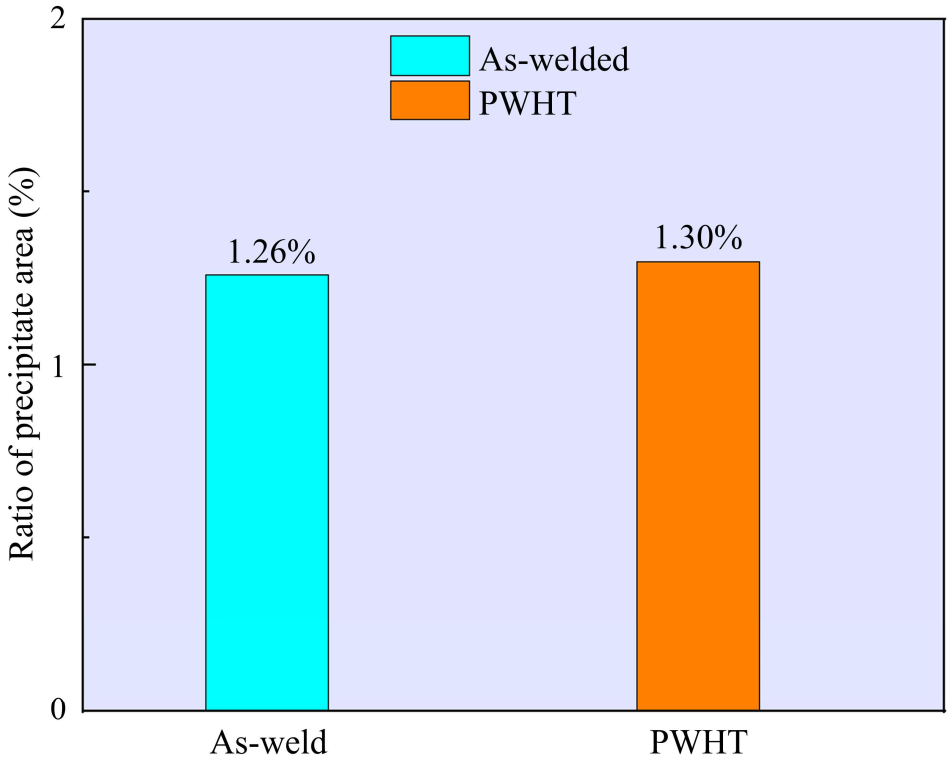

Figure 6. Density of intragranular precipitate.

3.2. Precipitated phases

Figure 7a,b show SEM images of as-welded cladding metal. Clear grain boundaries and interdendritic regions are observed. The grain boundaries appear straight or smoothly curved, while the interdendritic areas, which solidified last between dendritic arms, are enriched in alloying elements and impurities due to solute segregation. Many precipitated phases precipitated along the interdendritic region, and some particles precipitated near the grain boundaries, exerting a pinning effect. In addition, there are also precipitated phases at the grain boundaries. The intragranular precipitated phases are irregular in shape, such as strips or blocks. EDS analysis results of these precipitates are shown in Table 3. Compared with the matrix, these phases were enriched in Nb, Ti, and C elements. According to previous research, they were confirmed as (Nb,Ti)C carbides [11,12], with sizes lower than 3 μm. Furthermore, certain (Nb,Ti)C carbides were observed to nucleate and grow on the surface of Al_2O_3 oxides. Notably, Al_2O_3 exhibits a darker contrast than (Nb,Ti)C under observation. A comparable phenomenon was also reported by Huang in the deposited metal of ENiCrFe-9 [17]. It is well-known that aluminum (Al) acts as a highly effective deoxidizing element in a weld strip. During the welding process, the deoxidizing agent Al reacts with oxygen (O) to form aluminum oxides, which are subsequently incorporated into the slag phase. However, a small fraction of these oxides remained in the molten pool and became concentrated in the interdendritic areas, as dendritic arms grew during the solidification process. Ultimately, these oxides acted as nucleation sites for (Nb,Ti)C carbides, indicating that these oxides acted as heterogeneous nucleation sites during solidification. Further, the grain boundary precipitates were clearly observed under high magnification, and they appeared as fine granular particles. According to the reported literature, these particles have been characterized as

Cr-rich $M_{23}C_6$ carbides [18,19]. Compared with (Nb,Ti)C, $M_{23}C_6$ precipitated from the solid-state matrix at the grain boundaries at a lower temperature.

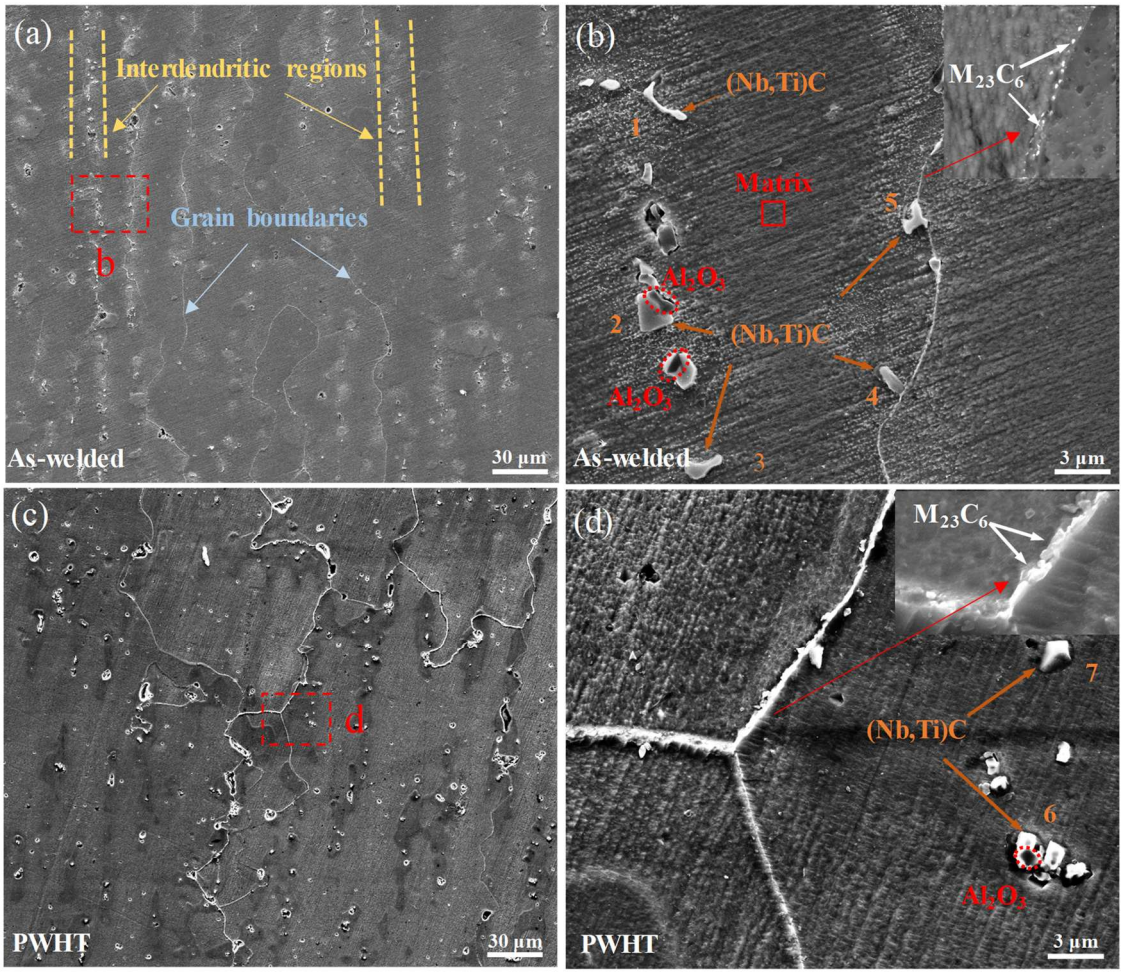

Figure 7. Precipitates of cladding metals: (a, b) as-welded state; (c, d) PWHT state.

The matrix microstructure of the nickel-based alloy is composed of γ-austenite. Meanwhile, the weld strip contains N band Ti elements, both of which show a tendency toward segregation. The sequence of solidification reactions occurring in the cladding metal could be outlined as follows [20–22]: initially, an L→γ solidification transformation occurred, during which dendrites formed, while Nb and Ti elements segregated and enriched in the interdendritic regions. Subsequently, when the enrichment of Nb and Ti reached a critical level, a eutectic reaction L→γ + (Nb,Ti)C occurred, which depleted the greater part of the accessible carbon. Given that Nb and Ti have identical crystal lattice structures and exhibit comparable atomic radii, they can form a complete solid solution with each other (i.e., unlimited solid solubility). Additionally, $M_{23}C_6$ carbides precipitate within the matrix at the grain boundaries at a temperature lower than that required for (Nb,Ti)C formation.

The SEM micrographs of the PWHT cladding metal are presented in Figure 7c,d. Compared with the as-welded cladding metal, the intragranular precipitates in the PWHT sample were still composed of (Nb,Ti)C carbides, including those precipitated on Al_2O_3 oxides, and no other secondary phases were detected. However, the morphology of $M_{23}C_6$ carbides at the grain boundaries changed from fine granular to blocky, which indicated the growth of $M_{23}C_6$ carbides during PWHT. The formation of

$M_{23}C_6$ carbides follows a diffusion-controlled mechanism, which is highly dependent on temperature and the diffusion behavior of alloying elements. During the prolonged holding at 610 °C, elements such as Cr and iron (Fe) diffuse along the grain boundaries, contributing to the growth of $M_{23}C_6$ [23].

After PWHT, the intragranular (Nb,Ti)C carbides maintained their morphology and distribution, demonstrating excellent thermal stability. In contrast, the intergranular $M_{23}C_6$ carbides experienced marked coarsening, evolving from fine granular precipitates to a blocky morphology. The superior stability of the (Nb,Ti)C carbides is ascribed to their slow precipitation kinetics [24]. Nevertheless, the coarsening of grain boundary carbides is likely to degrade grain boundary cohesion, consequently impairing the alloy's plasticity and toughness.

Table 3. EDS results of precipitated phases (wt.%).

Cladding metal	Sites	C	Si	Mn	Cr	Fe	Nb	Ti	Al	O	Ni
As-welded	1	17.14	0.39	1.22	11.55	3.66	47.98	0.20	-	-	17.85
	2	13.42	0.23	0.53	5.15	1.40	61.34	0.47	4.26	6.81	6.40
	3	14.07	0.24	0.96	7.62	2.19	63.47	0.27	-	-	11.17
	4	15.06	0.33	1.03	9.99	2.96	56.51	0.33	-	-	13.79
	5	15.70	0.34	1.40	11.14	3.43	50.28	0.35	-	-	17.36
	Matrix	2.13	0.76	2.08	29.38	7.86	2.01	-	-	-	55.78
PWHT	6	12.08	0.24	0.72	6.77	1.63	46.62	0.73	6.93	12.52	11.76
	7	13.18	-	-	2.47	0.42	74.10	1.12	-	-	3.15

3.3. Tensile properties

Figure 8 shows the room-temperature tensile properties of cladding metals in both as-welded and PWHT states. For the as-welded cladding metal, its yield strength, tensile strength, and elongation were 364 MPa, 578 MPa, and 51%, respectively; in contrast, the PWHT cladding metal had a yield strength of 380 MPa, a tensile strength of 589 MPa, and an elongation of 47%. The tensile strength of cladding metal increased by 11 MPa, whereas the elongation decreased by 4% after PWHT. This strength enhancement and plasticity reduction might be attributed to the $M_{23}C_6$ carbide changes at the grain boundaries after PWHT. Discontinuous $M_{23}C_6$ carbides functioned to pin grain boundaries and hamper the slip of dislocations, which led to the formation of dislocation tangles during tensile deformation [25,26]. With an increase in the amount of $M_{23}C_6$ carbides, the strength of the alloy was enhanced. Meanwhile, a localized stress field tended to develop around the $M_{23}C_6$ carbides. When the stress concentration around these carbides reached a critical level, plastic deformation became difficult to sustain, ultimately triggering crack initiation and a subsequent decrease in plasticity [23]. Therefore, the slight improvement in strength can be attributed to the enhanced pinning effect on dislocations caused by the coarsened $M_{23}C_6$ carbides at the grain boundaries, which hinders plastic deformation. The reduction in elongation is associated with stress concentration around these carbides, which promotes the early initiation of microvoids.

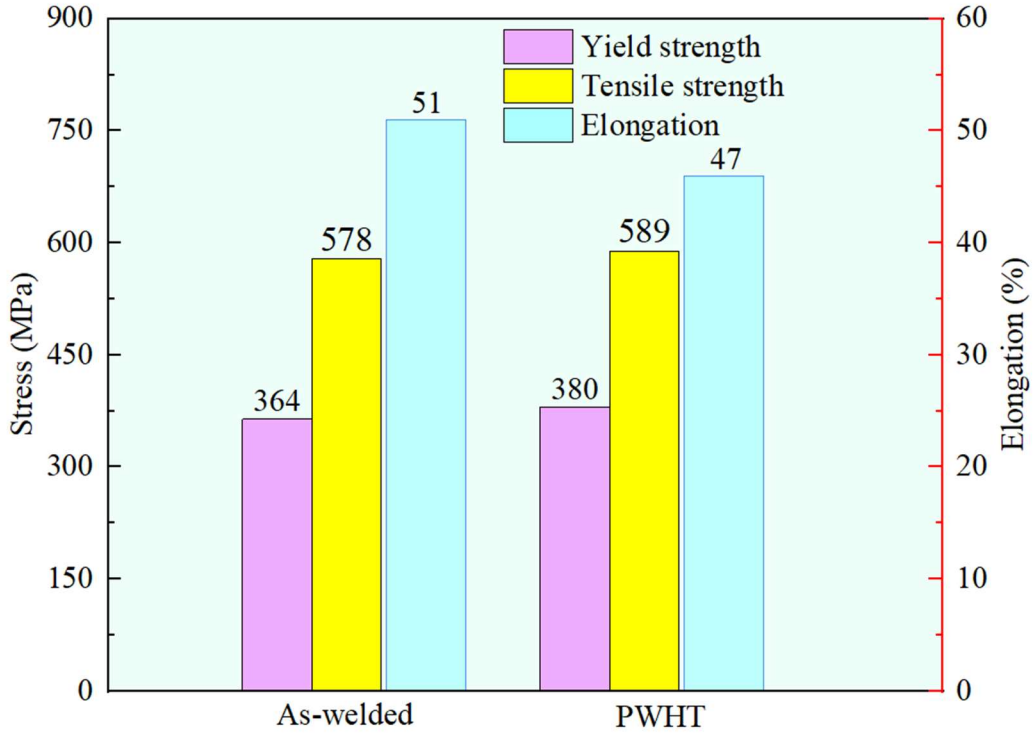

Figure 8. Tensile properties of cladding metals in as-welded and PWHT states.

Figure 9 presents the SEM micrographs of the tensile fracture surfaces of the cladding metal in the as-welded and PWHT states. A large number of dimples were distributed on the fracture surfaces, which was a typical characteristic of ductile fracture. Additionally, some secondary phase particles were observed within these dimples. The formation mechanism of dimples is closely associated with the nucleation, growth, and coalescence of microcavities during plastic deformation. Specifically, these precipitated phases act as nucleation sites for voids during the fracture process. Under tensile stress, dislocations accumulate around the precipitated phases, leading to localized stress concentration; this further promotes the initiation of microcavities at the interface between the precipitated phases and the matrix. As plastic deformation proceeds, the microcavities grow and interconnect, ultimately resulting in fracture. Further observation revealed that the dimples in the as-welded sample were larger and deeper (Figure 9b), which was indicative of good plastic deformation capacity. In contrast, the PWHT sample exhibited smaller and shallower dimples (Figure 9d), suggesting a reduced ability for micro-void coalescence during fracture and a lower reserve of plasticity. The fractographic analysis result was consistent with the elongation.

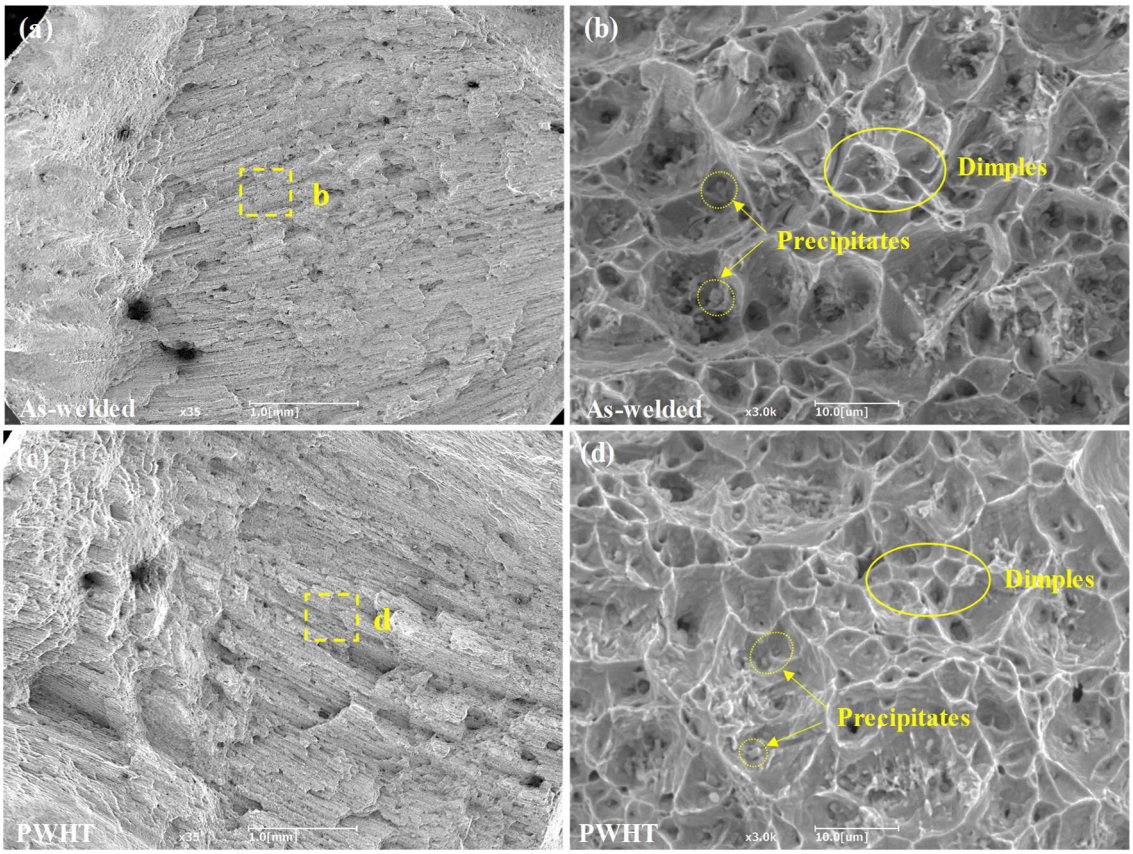

Figure 9. Fracture surfaces of tensile samples: (a, b) as-welded condition; (c, d) PWHT condition.

3.4. Impact toughness

The impact toughness at room temperature of cladding metals in the as-welded state and after PWHT is illustrated in Figure 10. The impact-absorbed energy of the as-welded metal was 79 J, whereas that of the PWHT metal was 75 J. After PWHT, the impact toughness decreased slightly, a trend consistent with the change in plasticity observed earlier. Figure 11 presents the impact fracture surfaces of the specimens under these two different conditions. Both fracture surfaces exhibited a typical dimple fracture morphology, indicative of ductile fracture. However, compared to the as-welded condition (Figure 11b), the dimples in the PWHT condition (Figure 11d) were relatively shallower; additionally, a certain number of secondary cracks were observed on the PWHT fracture surface (Figure 11c). This difference in fracture characteristics may be attributed to the coarsening of $M_{23}C_6$ carbides at the grain boundaries. The blocky $M_{23}C_6$ carbides, which are inherently brittle and exhibit a significant elastic modulus mismatch with the matrix, show limited deformability to coordinate with the matrix during impact loading. This leads to the formation of localized high-stress zones around the carbides; consequently, new crack sources are generated near the primary cracks, ultimately resulting in the formation of secondary cracks.

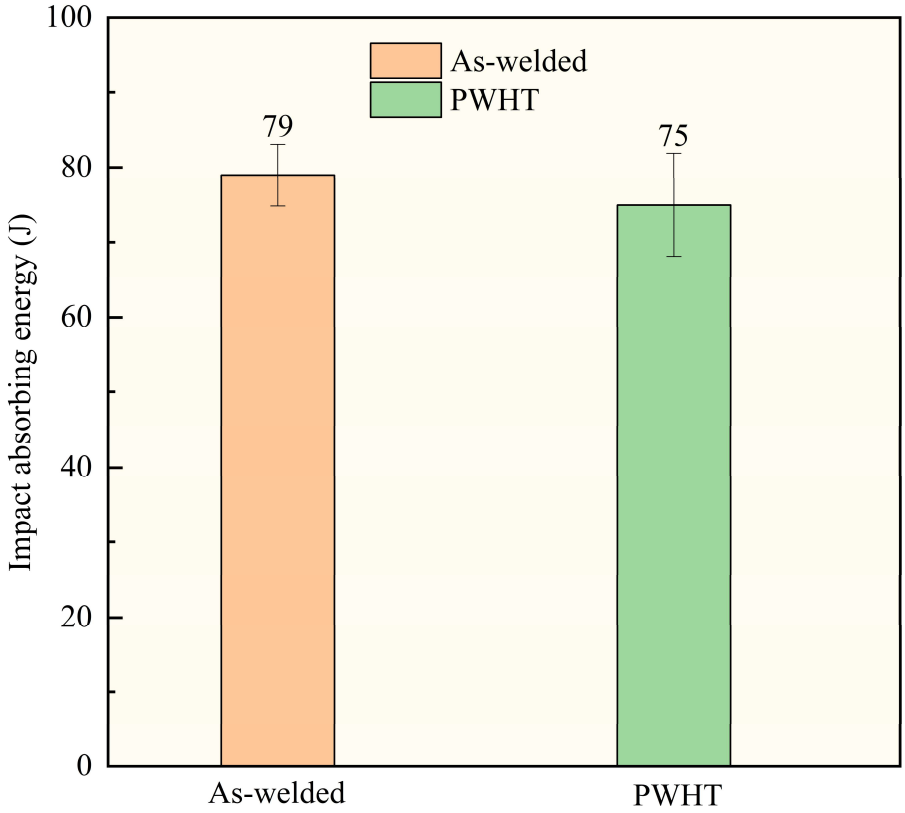

Figure 10. Impact-absorbing energy of as-welded and PWHT cladding metals.

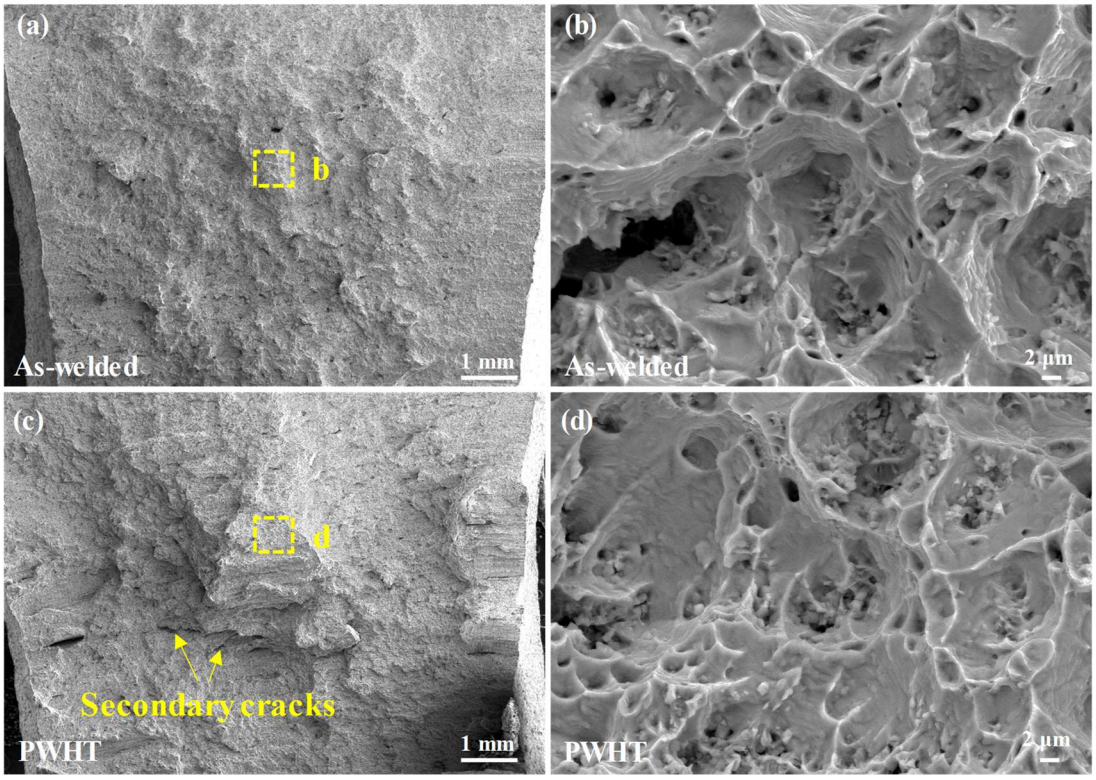

Figure 11. Fracture surfaces of impact samples: (a, b) as-welded state; (c, d) PWHT state.

4. Conclusions

The influence of PWHT at 610 °C for 24 h on the microstructure and mechanical properties of alloy 52M cladding metal fabricated by strip electrode SAW was studied. The main conclusions are as follows:

(1) The as-welded cladding metal showed a cellular solidification structure that remained unchanged after PWHT, confirming the thermal stability of the grains under the applied heat treatment parameters.

(2) The cladding metal contained intragranular (Nb,Ti)C and intergranular $M_{23}C_6$ carbides. After PWHT, the $M_{23}C_6$ carbides at grain boundaries coarsened markedly, changing from fine granules to blocky particles, while the (Nb,Ti)C carbides remained stable in morphology and distribution.

(3) During PWHT, $M_{23}C_6$ carbides coarsened, leading to a slight increase in tensile strength but a decrease in elongation and impact toughness. The coarsened carbides strengthened the metal by pinning grain boundaries but also caused embrittlement by promoting crack initiation.

Use of AI tools declaration

The authors declare they have not used Artificial Intelligence (AI) tools in the creation of this article.

Acknowledgments

This work was supported by the National Natural Science Foundation of China (Grant No. 52105351) and Natural Science Foundation of the Higher Education Institutions of Jiangsu Province (Grant No. 24KJA460002).

Author contributions

Haiyang Zhu: writing-original draft, conceptualization; Zuojin Qin: data curation, writing-review & editing; Changzheng Xu: supervision, formal analysis; Kun Liu: methodology, funding acquisition; Jiasheng Zou: project administration, funding acquisition.

Conflict of interest

The authors declare no conflict of interest.

References

1. Abdallah KAA, Namgung I (2016) Sensitivity study of APR-1400 steam generator primary head stay cylinder and tube sheet thickness. *Ann Nucl Energy* 92: 8–15. https://doi.org/10.1016/j.anucene.2016.01.021
2. Jia W, Ren L, Xu J, et al. (2022) Study on the relationship between Fe_3O_4 fouling and $NiFe_2O_4$ oxide layer in the secondary circuit of nuclear steam generator. *Surf Sci* 717: 122001. https://doi.org/10.1016/j.susc.2021.122001

3. Huang T, Zhang G, Liu F (2018) Design, manufacturing and repair of tube-to-tubesheet welds of steam generators of CPR1000 units. *Nucl Eng Des* 333: 55–62. https://doi.org/10.1016/j.nucengdes.2018.04.003
4. Hur DH, Choi MS, Lee DH, et al. (2013) Corrosion inhibition of steam generator tubesheet by alloy 690 cladding in secondary side environments. *J Nucl Mater* 442: 326–329. https://doi.org/10.1016/j.jnucmat.2013.09.023
5. Gong Y, Du MY, He GQ, et al. (2020) Failure analysis and prevention of corrosion occurring during storage on steam generator tube sheet for advanced PWR, Part II: Corrosion prevention design. *Eng Failure Anal* 115: 104688. https://doi.org/10.1016/j.engfailanal.2020.104688
6. Khan MS, Lourenço JC, Faria MIST, et al. (2023) Improving the corrosion resistance of Inconel 52M laser-cladded steel. *J Manuf Process* 106: 506–519. https://doi.org/10.1016/j.jmapro.2023.10.003
7. Yang C, Kim D, Lee H (2021) Carbide behavior and micro-void of Inconel 690 according to Nb content and aging temperature. *Met Mater Int* 27: 4681–4699. https://doi.org/10.1007/s12540-021-01028-0
8. Takaaki M, Hiroto Y, Kenji H, et al. (2013) Development of welding methods for dissimilar joint of alloy 690 and stainless steel for PWR components. *IHI Eng Rev* 45: 39–43.
9. Xu X, Pan D, Li E, et al. (2025) Nano-micrometer scale characterization of PWSCC crack tips in the transition zone of 52M overlay and the implication to intergranular cracking. *J Nucl Mater* 603: 155400. https://doi.org/10.1016/j.jnucmat.2024.155400
10. Li G, Zhang ML, Huang J, et al. (2015) A comparative study on microstructure and properties of Inconel 52M overlays deposited by laser beam and GTA cladding. *J Adv Manuf Technol* 81: 103–112. https://doi.org/10.1007/s00170-015-7198-8
11. Xu X, Jia Y, Pan D, et al. (2024) Effect of material chemical composition on oxidation and stress corrosion cracking of the submerged arc welding alloy 52M overlay in a simulated PWR primary water. *J Nucl Mater* 588: 154753. https://doi.org/10.1016/j.jnucmat.2023.154753
12. Li G, Zhang ML, Huang J, et al. (2015) Studies of electroslag cladding Inconel 52M multilayer. *Surf Sci* 31: 52–57. https://doi.org/10.1179/1743294414y.0000000388
13. Saha MK, Das S (2016) A review on different cladding techniques employed to resist corrosion. *J Assoc Eng* 86: 51–63. https://doi.org/10.22485/jaei/2016/v86/i1-2/119847
14. Xu X, Pan D, Zheng Y, et al. (2025) Effects of post-weld heat treatment on nanoscale microstructural degradation and primary water stress corrosion cracking resistance of submerged-arc-welded alloy 52M overlays. *Corros Sci* 256: 113213. https://doi.org/10.1016/j.corsci.2025.113213
15. Xu X, Pan D, Zhang K, et al. (2024) Ameliorating dilution of Cr and Ni and improving PWSCC resistance of 52M overlay by hot wire plasma arc cladding. *J Mater Res Technol* 31: 1392–1408. https://doi.org/10.1016/j.jmrt.2024.06.129
16. Kou S (2003) *Welding Metallurgy*, 2 Eds., New York: John Wiley & Sons.
17. Wang H, He G (2016) Effects of Nb/Cr on the cryogenic impact toughness of the deposited metal of ENiCrFe-9. *Mater Sci Eng A* 672: 15–22. https://doi.org/10.1016/j.msea.2016.06.067
18. Chen JQ, Lu H, Cui W, et al. (2014) Effect of grain boundary behaviour on ductility dip cracking mechanism. *Mater Sci Technol* 30: 1189–1196. https://doi.org/10.1179/1743284713y.0000000431

19. Luo L, Wei X, Chen J (2019) Grain boundary carbides evolution and their effects on mechanical properties of Ni 690 strip weld metal at elevated temperature, In: Chen S, Zhang Y, Feng Z, *Transactions on Intelligent Welding Manufacturing. Transactions on Intelligent Welding Manufacturing*, Singapore: Springer. https://doi.org/10.1007/978-981-10-8740-0_4
20. DuPont JN, Notis MR, Marder AR, et al. (1998) Solidification of Nb-bearing superalloys: Part I. Reaction sequences. *Metall Mater Trans* A 29: 2785–2796. https://doi.org/10.1007/s11661-998-0319-3
21. Ahn HI, Jeong SH, Cho HH, et al. (2019) Ductility-dip cracking susceptibility of Inconel 690 using Nb content. *J Alloys Compd* 783: 263–271. https://doi.org/10.1016/j.jallcom.2018.12.208
22. Ramirez AJ, Lippold JC (2004) High temperature behavior of Ni-base weld metal: Part I. Ductility and microstructural characterization. *Mater Sci Eng A* 380: 259–271. https://doi.org/10.1016/j.msea.2004.03.074
23. Tian W, Wu D, Li Y, et al. (2022) Precipitation behavior and mechanical properties of a 16Cr-25Ni superaustenitic stainless steel weld metal during post-weld heat treatment. *Acta Metall Sin* 35: 577–590. https://doi.org/10.1007/s40195-021-01274-6
24. Bao G, Yamamoto M, Shinozaki K (2009) Precipitation and Cr depletion profiles of Inconel 182 during heat treatments and laser surface melting. *J Mater Process Technol* 209: 416–425. https://doi.org/10.1016/j.jmatprotec.2008.02.021
25. Lee TH, Suh HY, Lee JH (2021) Precipitation behavior of $M_{23}C_6$ carbides and its effect on mechanical properties of Ni-based alloy 690. *J Nucl Sci Technol* 58: 45–50. https://doi.org/10.1080/00223131.2020.1797595
26. Jiang J, Zhu L (2012) Strengthening mechanisms of precipitates in S30432 heat-resistant steel during short-term aging. *Mater Sci Eng A* 539: 170–176. https://doi.org/10.1016/j.msea.2012.01.076

AIMS Press